Remote Sensing of Environment 152 (2014) 318–332

Contents lists available at ScienceDirect

Remote Sensing of Environment

journal homepage: www.elsevier.com/locate/rse

Generating Global LAnd Surface Satellite incident shortwave radiation and photosynthetically active radiation products from multiple satellite data

Xiaotong Zhang [a,*], Shunlin Liang [a,b], Gongqi Zhou [a,c], Haoran Wu [a,c], Xiang Zhao [a]

[a] State Key Laboratory of Remote Sensing Science, College of Global Change and Earth System Science, Beijing Normal University, Beijing 100875, China
[b] Department of Geographical Sciences, University of Maryland, College Park, MD 20742, USA
[c] State Key Laboratory of Remote Sensing Science, School of Geography and Remote Sensing, Beijing Normal University, Beijing 100875, China

ARTICLE INFO

Article history:
Received 12 November 2013
Received in revised form 9 July 2014
Accepted 9 July 2014
Available online 30 July 2014

Keywords:
Global irradiance
Photosynthetically active radiation
Shortwave radiation

ABSTRACT

Incident shortwave radiation (ISR) at the surface is an essential parameter in the land surface radiation budget and in many land surface process models. Incident photosynthetically active radiation (PAR) is required by nearly all terrestrial ecosystem models. Although several global radiation products from numeric models and satellite observations have been released, their coarse spatial resolutions and low accuracy, especially at high altitude regions, limit their applications in land community. In this study, the Global LAnd Surface Satellite (GLASS) ISR and PAR products are developed based on an improved look-up table method from 2008 to 2010 at a 5 km spatial resolution and a 3 hour temporal resolution, the first global radiation products at such high resolutions, from multiple polar-orbiting and geostationary satellite data, including the Moderate Resolution Imaging Spectroradiometer (MODIS), the Meteosat Second Generation (MSG2) SEVIRI, the Multi-functional Transport Satellite (MTSAT)-1R, and the Geostationary Operational Environmental Satellite (GOES) Imager. The look-up table algorithm primarily considers the influences of surface elevation, atmospheric water vapor because sensitivity experiments indicate that ISR and PAR are more sensitive to surface elevation, and less sensitive to atmospheric profiles and ozone amount. The water vapor absorption has strong impact on ISR but weak on PAR. Moreover, the surface bi-directional reflectance distribution function (BRDF) is taken into account to retrieve spatially and temporally continuous surface reflectances from the geostationary satellite observations, which is an input parameter in the revised look-up table method. Ground-based measurement data from 34 sites are used to validate the improved algorithm and the GLASS products. The validation results of the instantaneous ISR and PAR products at all validation sites are notably good with coefficient of determination values of 0.83 and 0.84, respectively, and root mean square error values of 115.0 Wm^{-2} and 49.0 Wm^{-2}, respectively. We also aggregate the GLASS ISR product for comparing with the corresponding ISCCP and CERES data at 7 SURFRAD sites and demonstrate that the GLASS ISR product is more accurate. The GLASS ISR and PAR products have been made publicly available.

1. Introduction

Incident shortwave radiation (ISR) from 0.3 to 3 μm at the land surface is an important parameter in the surface radiation budget (SRB) (Liang et al., 2006; Lu, Liu, Liu, & Liang, 2010) and drives the weather processes through latent and sensible heat fluxes and longwave emission, ultimately influencing the Earth's climate system (Wang, Dickinson, Wild, & Liang, 2010a, 2010b; Wu, Zhang, Liang, Yang, & Zhou, 2012). Similarly, incident photosynthetically active radiation (PAR) from 0.4 to 0.7 μm is a crucial parameter in ecosystem and climate change models by controlling the exchange of water vapor and carbon dioxide between vegetation and atmosphere (Frouin & McPherson, 2012; Frouin, McPherson, Ueyoshi, & Franz, 2012). Moreover, PAR is an indispensable parameter for the estimation of the gross primary production (GPP) or the net primary production (NPP) (Liang et al., 2006; Running, Nemani, Glassy, & Thornton, 1999; Running, Thornton, Nemani, & Glassy, 2000). Knowledge of the spatial and temporal distributions of PAR is essential to elucidating the biogeochemical cycles of carbon, nutrients, and oxygen (Liang et al., 2006; Van Laake & Sanchez-Azofeifa, 2004).

Currently, there are several surface radiation measurement networks, such as the Global Energy Balance Archive (GEBA) (Gilgen & Ohmura, 1999), the Baseline Surface Radiation Network (BSRN) (Ohmura et al., 1998),the Surface Radiation Budget Network (SURFRAD) (Augustine, Deluisi, & Long, 2000; Augustine, Hodges,

* Corresponding author.
E-mail address: xtngzhang@bnu.edu.cn (X. Zhang).

http://dx.doi.org/10.1016/j.rse.2014.07.003
0034-4257/

Cornwall, Michalsky, & Medina, 2005), the Atmospheric Radiation Measurement (ARM), the GEWEX Asia Monsoon Experiment (GAME/AAN), the Greenland Climate Network (GC-net), and the FLUXNET (Baldocchi et al., 2001). However, the networks provide relatively few surface radiation measurements in the high altitude areas (Liang, Wang, Zhang, & Wild, 2010; Van Laake & Sanchez-Azofeifa, 2004), and a worldwide observation network for incident PAR has not been established (Yang, He, Tang, Qin, & Cheng, 2010). Thus, modeling techniques using meteorological and remote sensing measurements are the practical methods for mapping ISR and PAR due to their large spatial coverage and scales (Liang et al., 2010). The ground-based networks can help identify the source of radiation budget errors in the SRB parameters derived from the developed models or the global circulation models (GCMs) (Gautier, Diak, & Masse, 1980; Liang et al., 2006).

There have been many reports on ISR estimation from the relative sunshine duration hours and other meteorological data (Angstrom, 1924; Muneer, Younes, & Munawwar, 2007; Paulescu & Schlett, 2003; Psiloglou & Kambezidis, 2007; Yang et al., 2010). The most widely used method is the relative sunshine hour duration method proposed by Angstrom (1924) and has been implemented and evaluated in various regions, however, the coefficients of these developed models are always site-dependent (Liu et al., 2009; Yang et al., 2010). In addition to the relative sunshine duration hour models, the ISR can also be obtained from other meteorological data such as temperature (Meza & Varas, 2000). Similar to the ISR retrieval, PAR can also be estimated from the relative sunshine duration hours and meteorological data. Qin, Yang, Liang, and Tang (2011) developed a method to estimate the daily mean PAR under all sky conditions based on relative sunshine data and the validated results at 7 SURFRAD stations indicate that the PAR estimation based on the relative sunshine duration hours is reasonable.

Besides the ground-based radiation models, satellite remote sensing is an alternative method for mapping both ISR and PAR at the regional and global scales (Cano et al., 1986; Harries et al., 2005; Laszlo et al., 2008; Liang et al., 2007; Liu, Liang, He, Liu, & Zheng, 2008; Mueller, Matsoukas, Gratzki, Behr, & Hollmann, 2009; Olofsson, Van Laake, & Eklundh, 2007; Pinker & Laszlo, 1992; Ryu, Kang, Moon, & Kim, 2008; Shahi et al., 2010; Van Laake & Sanchez-Azofeifa, 2004; Zhang, Rossow, & Lacis, 1995; Zhang, Rossow, Lacis, Qinas, & Mishchenko, 2004; Zheng, Liang, & Wang, 2008). Currently, there are several satellite-derived solar radiation products, such as the International Satellite Cloud Climatology Project — Flux Data (ISCCP-FD), the Clouds and the Earth's Radiant Energy System — Monthly Gridded Radiative Fluxes and Clouds (CERES-FSW), the Global Energy and Water-cycle Experiment — Surface Radiation Budget (GEWEX-SRB), and the Climate Monitoring Satellite Application Facility (CM-SAF) datasets.

Although long-term ISR and PAR products have been generated, their coarse spatial resolutions remain insufficient for land-surface models and other applications. Moreover, the validation results of the current radiation products are not as good as expected especially in highly polluted and high altitude areas. Gui, Liang, Wang, Li, and Zhang (2010) validated three satellite-based downward surface shortwave irradiance datasets (GEWEX-SRB, ISCCP-FD, and CERES-FSW) and demonstrated large biases in Southeast Asia, the Tibet Plateau, and Greenland. Thus, new global radiation products with greater accuracy and higher spatial resolution must be developed.

This paper presents the algorithms for generating the Global LAnd Surface Satellite (GLASS) ISR and PAR products from both polar-orbiting and geostationary satellite remote sensing data. The overview of the GLASS products has been recently published (Liang et al., 2013). The geostationary satellite data have a fine temporal resolution without covering high-latitude regions, but the polar-orbiting satellite data are of high frequency in those regions due to orbit convergence. Integrating both types of data enables the generation of high spatial and temporal resolution solar radiation products.

Table 1
A description of the site conditions.

Site	Network	Latitude	Longitude	Elevation (m)	Land cover
Bondville	SURFRAD	40.05	−88.37	213	Cropland
FortPeck	SURFRAD	48.31	−105.10	634	Grassland
Goodwin Creek	SURFRAD	34.25	−89.87	98	Pasture
Penn State	SURFRAD	40.72	−77.93	376	Cropland
Sioux Falls	SURFRAD	43.73	−96.62	473	Grassland
Boulder	SURFRAD	48.31	−105.24	1689	Grassland
Desert Rock	SURFRAD	36.63	−116.02	1007	Desert
ARM-SGP Main	AmeriFlux	36.61	−97.49	314	Grassland
Audubon Research Ranch	AmeriFlux	31.59	−110.51	1469	Grassland
Brookings	AmeriFlux	44.35	−96.84	510	Grassland
Fermi_Agricultural	AmeriFlux	41.86	−88.22	225	Cropland
Flagstaff Managed Forest	AmeriFlux	35.14	−111.73	2160	Forest
Flagstaff UnManaged Forest	AmeriFlux	35.09	−111.76	2180	Forest
Neustift	CarbonEuropeIP	47.12	11.32	1095	Forest
Lonzee	CarbonEuropeIP	50.55	4.74	165	Cropland
Vielsalm	CarbonEuropeIP	50.31	6.00	491	Forest
Laegeren	CarbonEuropeIP	47.48	8.37	645	Forest
Oensingen2 crop	CarbonEuropeIP	47.29	7.73	450	Cropland
Bily Kriz-Beskidy Mountains	CarbonEuropeIP	49.50	18.54	862	Forest
Bily Kriz grassland	CarbonEuropeIP	49.49	18.54	837	Forest
CZECHWET	CarbonEuropeIP	49.02	14.77	425	Cropland
Moldova	AERONET	47.00	28.82	205	Urban
Alta_Floresta	AERONET	−9.87	−56.10	277	Grassland
CEILAP-BA	AERONET	−34.57	−58.50	10	Grassland
Kherlenbayan Ulaan	AsiaFlux	47.02	108.73	1235	Grassland
Arou	COIRAS	38.04°	100.46°	3033	Grassland
Changwu	COIRAS	35.20	107.67	968	Grassland
Dayekou	COIRAS	38.53	100.25	2899	Grassland
Dingxi	COIRAS	35.56	104.59	1928	Grassland
Dongsu	COIRAS	44.09	113.57	1024	Grassland
Tongyu	COIRAS	44.57	122.88	153	Grassland
Yingke	COIRAS	38.86	100.41	1529	Cropland
Yuzhong	COIRAS	35.95	104.13	1794	Grassland
Zhangye	COIRAS	39.09	100.30	1456	Grassland

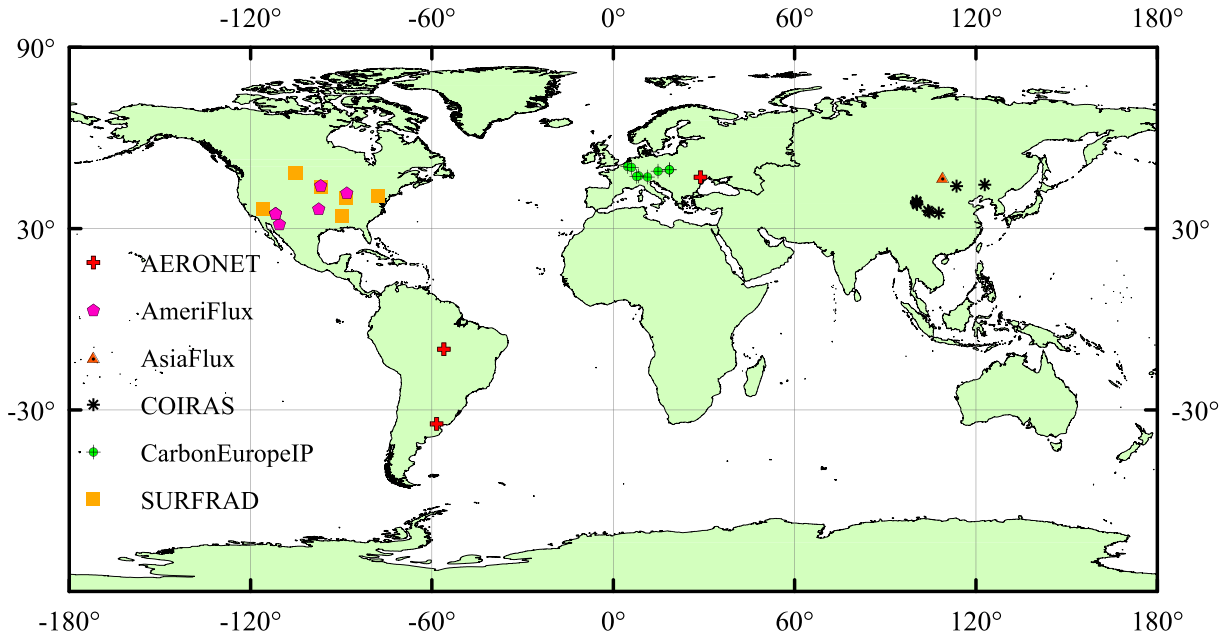

Fig. 1. The spatial distribution of 34 sites used in this study.

There are algorithms for estimating the solar radiation from individual satellite data, but this study is the first attempt to map ISR and PAR globally at a 5 km spatial resolution and a 3 hour temporal resolution from both MODIS, a polar-orbiting satellite sensor, and several geostationary satellite data, such as the Meteosat Second Generation (MSG) SEVIRI, the Multi-functional Transport Satellite (MTSAT)-1R, and the Geostationary Operational Environmental Satellite (GOES) Imager. We have also significantly refined the algorithms in several areas, explicitly considering the ozone and the water vapor absorption, surface elevation, and bi-directional reflectance distribution function (BRDF) effects. An extensive validation has also been performed. This paper is organized as follows: The ground measurements and satellite data used in this paper are introduced in Section 2; the implementation of the algorithms and the important related issues are discussed in Section 3; the global mapping and evaluation of ISR and PAR are shown in Section 4; and a short summary is provided at the end of this paper.

2. Data

2.1. In situ data

Ground measurements of ISR and PAR at 34 sites across the world are used for validation and their basic information is presented in Table 1. These sites are parts of surface radiation networks mentioned in the Introduction of this paper. The land cover types of these sites include cropland, grassland, urban, and forest. These sites are located in contrasting climatic zones, covering a wide latitude range from −35° to 50° and a longitude range from −120° to 120° as illustrated in Fig. 1. Ground measurements of ISR and PAR were collected every 3 min at the SURFRAD site. Incident PAR was measured every 2 min at the AERONET site, and ISR and PAR were released every 30 min at the Asiaflux, the Ameriflux, and the CarbonEuropeIP sites. The ISR and PAR were provided in thirty-minute averages at the COIRAS sites.

2.2. MODIS data

The MODIS sensors onboard the Terra and Aqua satellites have 36 spectral bands ranging from the visible to the thermal-infrared spectrum. The spatial resolution varies from 250 m (bands 1 and 2) to 500 m (bands 3 to 7) and 1000 m (band 8 to 36). The MODIS sensors view the entire Earth every 1 or 2 days. The top-of-atmosphere (TOA) radiance (MOD02 and MYD02) of the blue band (band 3) is used to calculate ISR and PAR in this study. Moreover, the MODIS geolocation dataset (MOD03 and MYD03), land surface reflectance product (MOD09A1) (Vermote, Saleous, & Justice, 2002), and the precipitable water product (MOD08_D3) are also used (Hubanks, King, Platnick, & Pincus, 2006). The geolocation dataset provides geodetic coordinates, ground elevation, solar and satellite zenith, and the azimuth angle for each 1 km MODIS sample. The land surface reflectance products (MOD09A1) provide an estimate of the surface spectral reflectance at a 500 m resolution and an 8-day gridded level-3 product. The MODIS atmospheric precipitable water product (MOD08_D3) is produced from near-infrared bands. Under cloudy conditions, the water vapor column above the clouds is used instead of the total water vapor amounts because the influence of the amount of water vapor on solar radiation, especially in the visible band, is not at the dominant position under cloudy conditions.

Table 2
The detailed information of the satellite data used in this study.

Sensors	Product	Spatial resolution	Temporal resolution	Map projection
MODIS	TOA radiance (MOD02&MYD02)	500 m	Instantaneous	Geographic Lat/Lon (swath)
	Geographical location (MOD03 &MYD03)	500 m	Instantaneous	Geographic Lat/Lon (swath)
	Surface reflectance (MOD09A1)	500 m	8 days	Sinusoidal
	Water vapor (MOD08)	1°	1 day	Geographic Lat/Lon (grid)
GOES11 imager	TOA radiance (visible band)	1 km	3 h	Geographic Lat/Lon (disk)
GOES12 imager	TOA radiance (visible band)	1 km	3 h	Geographic Lat/Lon (disk)
MSG2 SEVIRI	TOA radiance (visible band)	1 km	15 min	Geographic Lat/Lon (disk)
Mtsat-1r imager	TOA radiance (visible band)	1 km	1 h	Geographic Lat/Lon (grid)

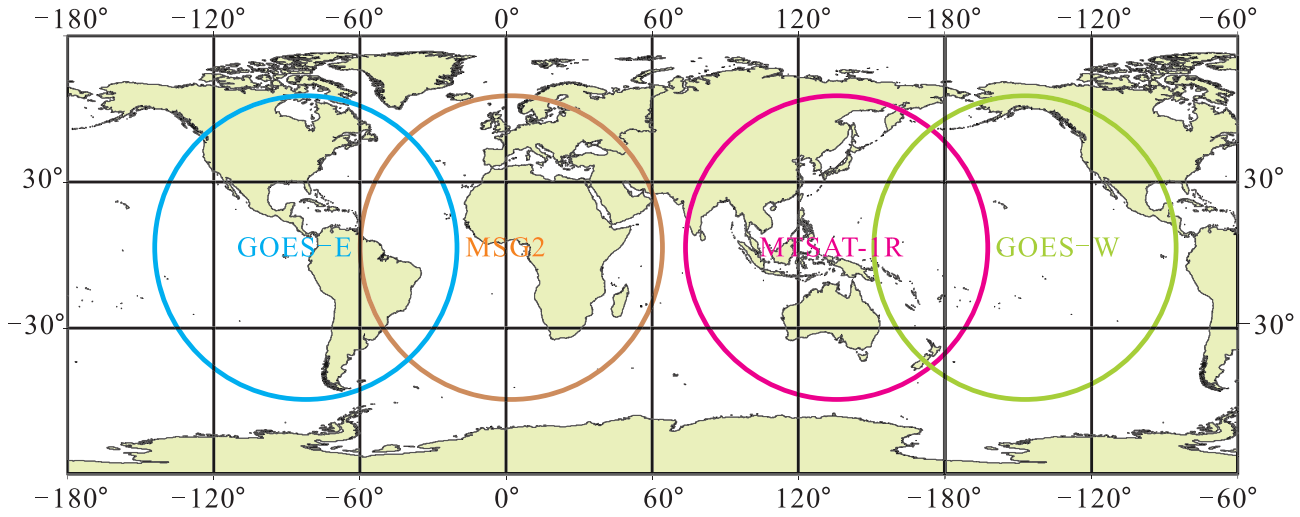

Fig. 2. The spatial coverage of the geostationary satellites used to generate global ISR and PAR in this study.

However, the influence of water vapor on the solar radiation estimation at the surface cannot be ignored under clear-sky conditions. The detailed information of the MODIS and the geostationary satellite data used in this study are summarized in Table 2.

2.3. Geostationary satellite data

The TOA radiance of geostationary satellite visible band data, including GOES11, GOES12, MSG2, and MTSAT-1r data, is used to generate ISR and PAR. The spatial coverage of the selected geostationary satellite is shown in Fig. 2. Although the satellites cover the latitude range from 60°S to 60°N across the world, missing gaps remain on the continent of Eurasia and the high latitude areas. Thus, both polar-orbiting and geostationary satellite data are used to ensure global coverage. GOES11 is designated GOES-West and is located at 135°W over the Pacific Ocean, whereas GOES12 is designated GOES-East and is located at 75°W over the Amazon River. The imaging instrument on the current GOES has one visible band and four bands in the infrared spectrum. The GOES imagers acquire observations with high spatial (≥1 km) and temporal resolutions (≥15 min) (Otkin, Anderson, Mecikalski, & Diak, 2005). The main payload of the MSG2 satellite carries an optical imaging radiometer called the Spinning Enhanced Visible and Infrared Imager (SEVIRI). SEVIRI collects images with 1 km spatial resolution at visible bands every 15 min, compared to three bands every 30 min for the comparable instrument on Meteosat. The Multi-functional Transport Satellite (MTSAT) series succeeds the Geostationary Meteorology Satellite (GMS) series. The MTSAT series satellites are located in a geostationary orbit 35,800 km above the equator at 140°E or 145°E. The MTSAT series carries a new imager with a new infrared channel (IR4) in addition to the four channels (VIS, IR1, IR2, IR3) of the GMS-5. The spatial resolution is 1 km (VIS) and 4 km (IR) at the sub-satellite point.

As shown in Table 2, the spatial resolution and the map projection of different satellite data or products are different. To generate global ISR and PAR with 5 km spatial resolution and to reduce the computational time, all of the satellite data utilized in this study are aggregated to 5 km spatial resolution. The MODIS TOA radiance data and geographical location data are converted to a sinusoidal projection to enable the direct use of the MODIS surface reflectance data, which are also provided in a sinusoidal projection. The geostationary satellite data are also converted to a sinusoidal projection to generate global ISR and PAR through the combination of MODIS-derived ISR and PAR with the corresponding data derived from the geostationary satellite.

3. Methodology

To obtain the global coverage, the ISR and PAR for each satellite data are first estimated, and then integrated. The flowchart of the algorithm is shown in Fig. 3. In the following sections, we will introduce the improved LUT method, and discuss more technical details.

3.1. The LUT method

The LUT method, proposed by Liang et al. (2006), attempts to establish the relationship between incident solar radiation at the surface with the TOA radiance measured by satellite sensors. Liang et al. (2006) developed the LUT approach for estimating instantaneous incident PAR from MODIS data and evaluated the retrieved PAR using ground measurements from 7 FLUXNET sites. Zheng et al. (2008) applied the LUT method to derive PAR using GOES data. An operational system was developed to generate instantaneous and daily PAR using MODIS data with several improvements by Liu et al. (2008), which included utilizing MODIS 1B data by combining MODIS land surface products and BRDF model parameters to estimate diffuse PAR, direct PAR, and total PAR and by removing the noise and cloud contamination of land surface reflectance. Lu et al. (2010) extended the LUT method to estimate ISR using GMS5 visible imagery. The retrieved daily PAR was compared with the ground measurements for one year at 96 stations in China with a correlation coefficient of ~0.9 and a bias of 1.5%. Compared with certain existing approaches, the LUT method requires only the parameters observed by remote sensing, instead of cloud and aerosol optical thickness, which require retrieval by more complex models, causing lager errors for ISR and PAR estimation.

Although the LUT method was used to estimate solar radiation especially PAR from individual satellite data, the global ISR and PAR products have not been generated based on the LUT method using multiple satellite data. Thus, we attempt to present an operational scheme to map ISR and PAR globally with an improved LUT method at a 5 km spatial resolution and a 3 hour temporal resolution from both MODIS, a polar-orbiting satellite sensor, and several geostationary satellite data in this study. The influences of surface elevation, atmospheric water vapor, and a surface bi-directional reflectance distribution function (BRDF) on ISR and PAR estimation are taken into account. The surface elevation is one of the important input parameters in the LUT. An empirical method is used for the water vapor correction of ISR. The BRDF parameters derived from the geostationary satellite "clearest" observations are used to estimate the surface reflectance under cloudy conditions. Two

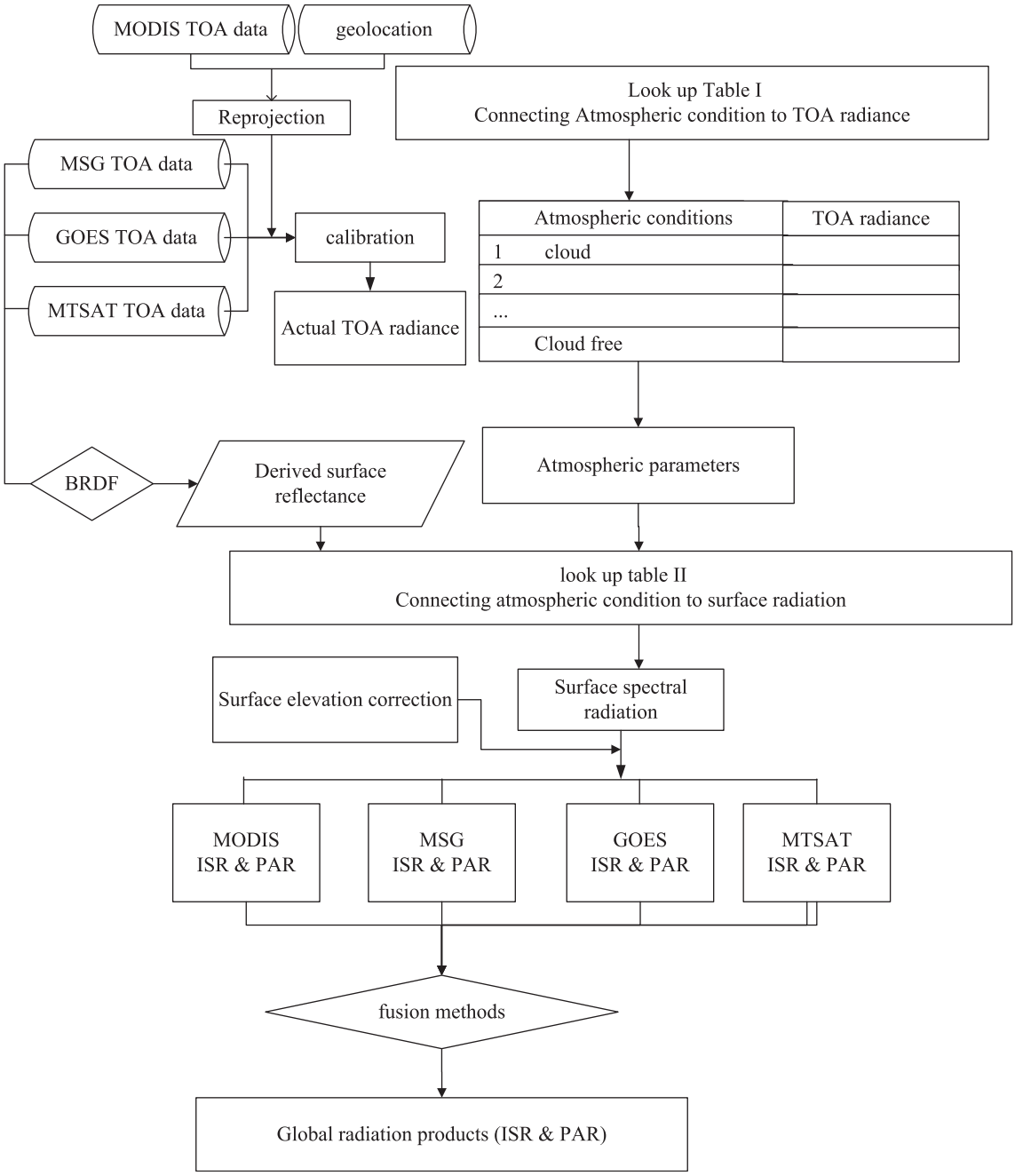

Fig. 3. The primary procedure of the LUT method used to generate global ISR and PAR products.

Table 3
Summary of crucial parameters for generating a look up table (LUT) through MODTRAN.

Input parameters	Values
Solar zenith angle	0°, 15°, 30°, 45°, 55°, 65°, 75, 85°, 90°
View zenith angle	0°, 20°, 40°, 60°, 80°
Relative azimuth angle	0°, 30°, 60°, 90°, 120°, 150°, 180°
Surface altitude	0.000 km, 1.500 km, 3.000 km, 4.500 km, 5.900 km
Aerosol type	Rural aerosol
Cloud type	Altostratus cloud
Aerosol loadings (visibility)	5, 10, 20, 30, 100 (km)
Cloud optical thickness	1, 2, 3, 5, 10, 25, 50, 70, 128 (km^{-1})
Water vapor amount	Default value
Ozone amount	Default value

look-up tables are created by integrating the visible band spectral response function in two steps for each sensor through radiative transfer simulation by MODTRAN (Anderson et al., 1999). The first table is used to compare the actual TOA reflectance with the simulated TOA reflectance to derive the atmospheric conditions; the second table is used to estimate the instantaneous ISR and PAR at the surface using the atmospheric conditions derived from the first look-up table. The detailed information of the parameters established for the creation of the two LUTs mentioned above during radiative transfer simulation is summarized in Table 3. The implementation of these two LUTs will be introduced in the following sections.

The look-up table works only when the output is linear with respect to changes in the independent variables and when the interactive effects of different variables are weak (Liang et al., 2006; Lu et al., 2010). To better evaluate the interactions of these atmospheric input variables

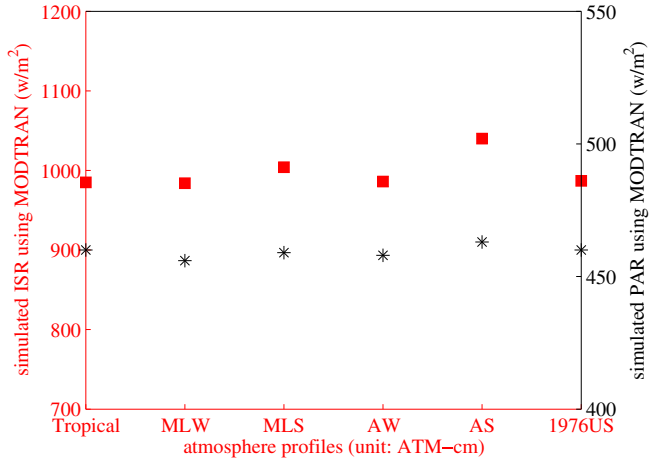

Fig. 4. Sensitivity of PAR and ISR estimates to atmosphere profiles. The atmospheric condition is represented by a mid-latitude winter atmosphere with a rural aerosol type. Other input atmospheric variables are set as constants (solar zenith angle, 0°; visibility, 90 km; surface albedo, 0.2; cloud extinction coefficient, 1 km^{-1}). Trp, MLW, MLS, AW, AS, and 1976US represent the tropical, mid-latitude winter, mid-latitude summer, Arctic winter, Arctic summer, and 1976 US standard atmosphere profiles, respectively.

in the LUT, a sensitivity analysis of the atmosphere profiles, ozone level, water vapor amount, surface elevation, and aerosol model is performed in the study. The six standard atmosphere profiles (tropical, midlatitude winter, midlatitude summer, sub-Arctic winter, sub-Arctic summer, and 1976 US standard) were employed with specified atmosphere variables. The influences of the atmosphere profiles on the estimation of ISR and PAR are illustrated in Fig. 4. The standard deviation (STD) of the simulated ISR and PAR values with selected atmosphere profiles is 22 Wm^{-2} and 2.2 Wm^{-2}, respectively. The large STD of the ISR is caused by the Arctic winter profiles; the STD is reduced to 7 Wm^{-2} when these atmosphere profiles are excluded. Thus, we can conclude that the ISR and PAR simulations are not sensitive to the atmosphere profiles for this algorithm, which is consistent with the results obtained by Liang et al. (2006).

The sensitivity experiments used to determine the dependence of ISR and PAR on ozone levels are shown in Fig. 5 at mid-latitude summer atmospheric profiles using a rural aerosol model under cloud-free conditions and a visibility of 90 km, which is considered a very clear atmospheric condition. The other atmospheric parameters are set as constants in MODTRAN. As shown in Fig. 5, the ISR and PAR estimates vary by approximately 30 Wm^{-2} and 20 Wm^{-2}, respectively, at the surface with the increasing ozone from 0.0 to 0.8 atm-cm. However, the amount of ozone does not change significantly under most conditions. Under other relatively hazy/cloudy air conditions, the influence of the ozone level is smaller. Thus, ozone is set as a constant in the simulation, and the effects of ozone are not corrected in our algorithm. The effects of water vapor on the estimation of ISR and PAR are also shown in Fig. 5. Water vapor has a significant effect on ISR but is insignificant in terms of the PAR calculation because the absorption of water vapor occurs primarily in the infrared band (Liu et al., 2008). Therefore, a simple water vapor correction function is applied to the ISR product.

The effects of surface elevation on ISR and PAR are also important and cannot be ignored, and there are many published reports on this topic (Dubayah, 1992; Wang, Zhou, Liu, & Sparrow, 2005). Surface elevation effects are a dimension considered in the look-up table in our algorithm. The variations in the ISR and PAR estimates with changes in the surface elevation are described in Fig. 6. We conclude that the influences of surface altitudes on ISR and PAR are significant under both cloudy conditions and cloud-free conditions and cannot be neglected. The surface elevation may cause an error of up to 100 Wm^{-2} and is a significant source of error in ISR and PAR estimation. For example, this effect is the most likely reason that a number of current radiation products have large errors over the Tibetan Plateau.

To evaluate the effects of aerosol models on ISR and PAR simulations using MODTRAN, we select four basic aerosol modes to represent atmospheric turbidity in MODTRAN. The sensitivities of ISR and PAR to selected aerosol modes (rural, maritime, urban, and tropospheric) under cloud-free conditions with 23 km of visibility are shown in Fig. 7; this comparison shows that ISR and PAR have similar sensitivities to the various aerosol modes. In addition, the rural, maritime, and tropospheric aerosol modes do not have a significant influence on ISR and PAR, whereas the urban aerosol mode does have an effect. The maritime and urban aerosol modes affect the largest difference, reaching approximately 60 and 29 Wm^{-2} for ISR and PAR, respectively, due to the strong absorption of solar radiation by urban aerosols. These results are consistent with the findings of Lu et al. (2010). The retrieval of ISR

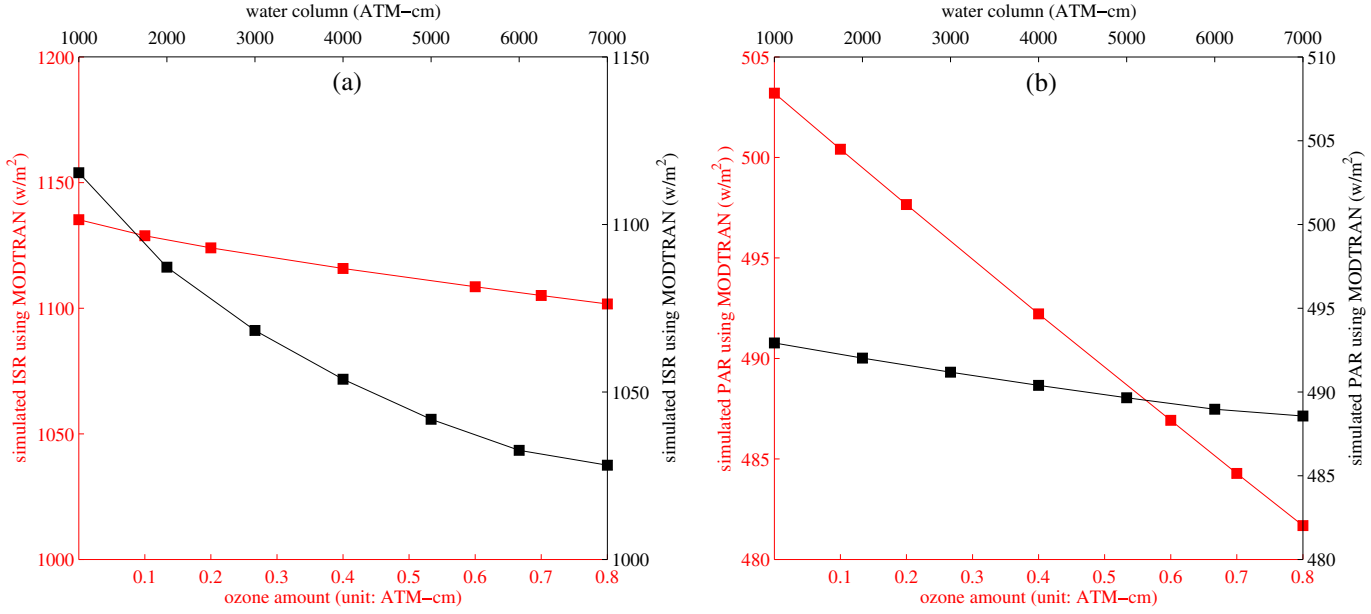

Fig. 5. Sensitivity of (a) ISR and (b) PAR to variations in the amounts of ozone and water vapor. The atmospheric condition is represented by a mid-latitude summer atmosphere with a rural aerosol type. Other input atmospheric variables are set as constants (water vapor amount, 2.0 gm/m^2; visibility, 90 km; albedo, 0.20).

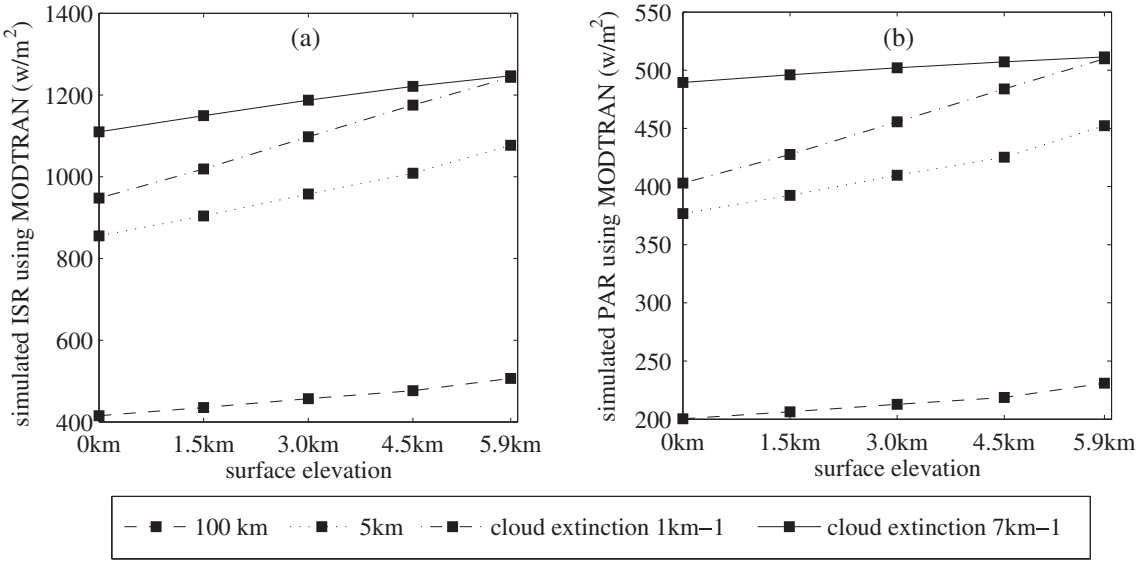

Fig. 6. Sensitivity of (a) ISR and (b) PAR at the surface to the surface altitude under different atmosphere conditions (100 km visibility, 5 km visibility, 1 km^{-1} cloud extinction, and 7 km^{-1} cloud extinction of mid-latitude summer atmosphere with a rural aerosol type).

and PAR is affected by the distinct characteristics and size distributions of different aerosol modes under cloud-free conditions, especially in highly polluted regions (Wang, Liang, Liu, & Zheng, 2010). However, the influences of the aerosol modes on the estimation of solar radiation at the surface are not implemented in this algorithm because the aerosol influences are insignificant under cloudy conditions and significant under clear-sky conditions.

3.2. ISR and PAR estimation based on the LUT

Once the two LUTs are generated through radiative transfer simulation, we can derive the ISR and PAR. The workflow for searching for the look-up tables is as follows. First, we calculate the TOA reflectance or radiance using the digital numbers (DNs) for the corresponding bands from the actual satellite observational data. Then, we either derive the surface reflectance data either from the MODIS land surface reflectance data (MOD09A1) or estimated through the kernel driven models for geostationary satellites, which will be described in detail in Section 3.3. Next, we calculate the TOA radiance for each atmospheric condition ranging from the clearest conditions (high surface meteorological range) to the cloudiest conditions (high cloud extinction coefficient) under certain geometries using the generated LUT at the satellite level. Then, the actual TOA radiance derived from the selected sensors' bands is compared with the calculated radiances under all of the atmospheric conditions and certain geometries using the TOA LUT to retrieve the atmospheric index, which is defined as the index of the atmospheric condition in the study. Finally, incident solar radiation at the surface can be obtained using the retrieved atmospheric index and the derived surface reflectance under certain geometries using the LUT at the surface level.

3.3. Determination of the surface reflectance

The determination of surface reflectance is one of the most important tasks for ISR and PAR estimation based on the LUT method. Because the characteristics are different for different sensors or satellites, the retrieval of the surface reflectance is divided into two types. The MODIS land surface reflectance products (MOD09A1) are used as the input parameters for the MODIS sensor. However, for geostationary satellites, the minimum TOA blue band reflectance method is employed to derive the surface reflectance (Liang et al., 2006). Although the MODIS MOD09A1 products provide the surface reflectance in an 8-day period

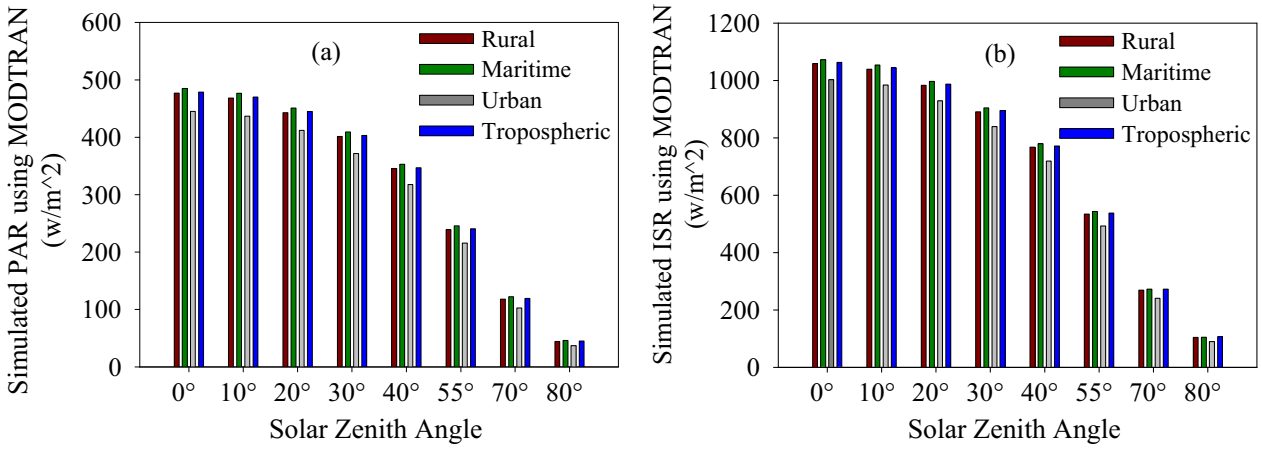

Fig. 7. Sensitivity of (a) PAR and (b) ISR to aerosol modes under different solar zenith angles. The atmospheric condition is represented by a mid-latitude summer atmosphere. Other input atmospheric variables are set as constants (water vapor, 2.0 gm/m^2; visibility, 23 km; albedo, 0.20).

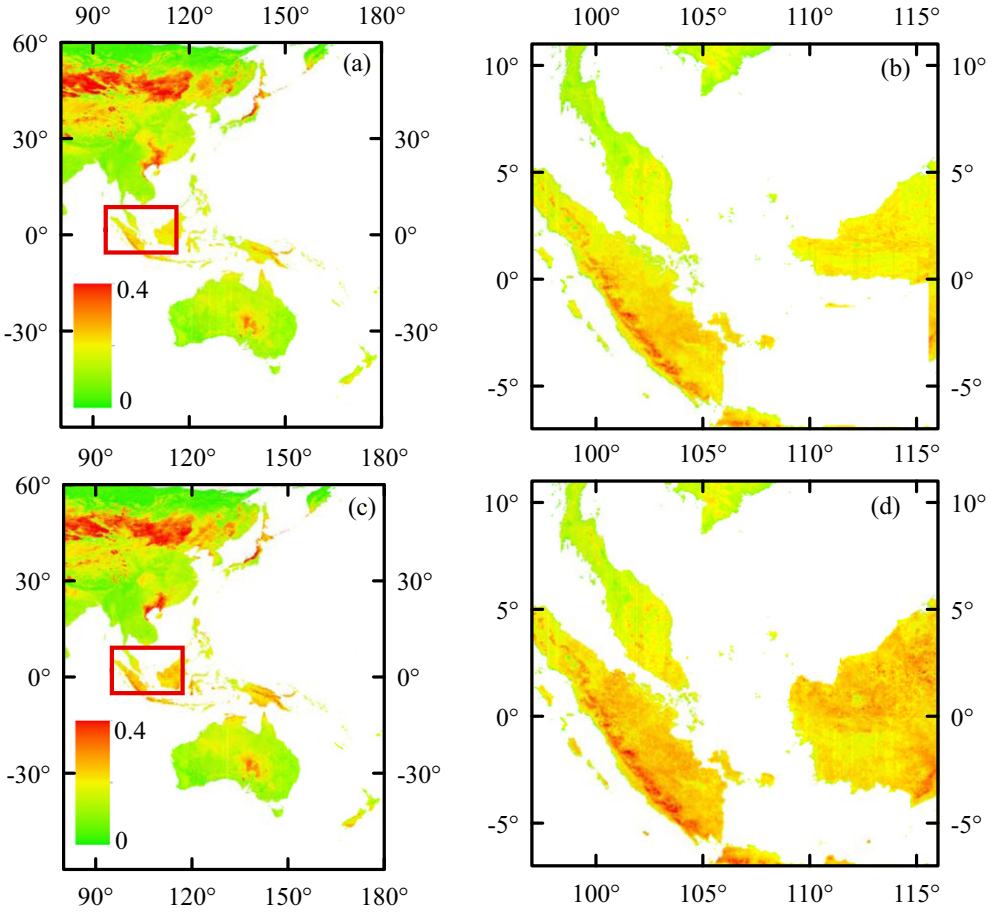

Fig. 8. The retrieved surface reflectances (visible band) using Mtsat-1r observations at GMT 00:30 on Jan 1st, 2008. (a) and (b) Results of the retrieved surface reflectances by using one month temporal window of the full and the subset image, respectively. (c) and (d) Results of the retrieved surface reflectances by using half of one month temporal window of the full and the subset image, respectively.

in the absence of clouds or cloud shadows and aerosol loadings, the surface reflectance for the MODIS sensor data remain contaminated by clouds. Thus, the MODIS 8-day composite land surface reflectance blue band data are processed using a time-series based method to reduce the influences of clouds and snow (Tang et al., 2013), and the processed data are then utilized to retrieve ISR and PAR.

For the geostationary satellite, the surface reflectance is obtained based on the "clearest" observation in the temporal dimension (assumed as 1 month in this study) for each pixel method proposed by Liang et al. (2006), which is based on the assumption that the surface reflectance can be determined by assuming the surface is a Lambertian reflector and the aerosol optical depths are known for the "clearest" observations. The clearest observations are identified on the basis of their minimal values in the visible bands. We convert the TOA radiance of the visible bands into apparent surface reflectance from the LUTs with a known aerosol visibility value for a very clear atmospheric condition (a 100 km meteorological visibility range is assumed in this study). The percentages of 15 of the total observations are identified as the clearest observations within the temporal window. The land surface properties may experience a large change during one month. The temporal window of 1–3 months is recommended by Liang et al. (2006). But we found that lots of detailed variation information of surface reflectances (e.g. snow) may be ignored if the temporal window is too long. Similarly, the surface reflectance may be contaminated by clouds if the temporal window is too short. In our experiments, we found that the temporal window of one month is more reasonable. Fig. 8(a) and (c) depicts the retrieved surface reflectances (visible band) by using one month and half of one month temporal windows for Mtsat-1r observations at GMT 00:30 on Jan 1st, 2008, respectively. We can draw that the differences of the retrieved surface reflectances by using one month and half of one month are small, but the retrieved results may be influenced due to clouds especially at the low latitude regions, as shown in Fig. 8. Here a fixed percentage (15%) of the total observations within the temporal window is used to determine the number of clear observations. Ideally, it should be variable both spatially and temporally. More experiments may be needed in the future. These lowest 15% surface reflectance values, derived for the "clearest" observations, are regarded as the actual surface reflectance to fit the RossThick-LiSparse model to characterize the surface bidirectional feature, which in turn will be utilized to calculate the surface reflectance for the observations taken under "hazy/cloudy" conditions. The RossThick-LiSparse model is a weighted function of the isotropic parameter and two kernels of viewing and illumination geometry. The weighted function is presented in the following Eq. (1) (Lucht, Schaaf, & Strahler, 2000).

$$\rho_\lambda(\theta_s,\theta_v,\phi_s-\phi_v) = f_{iso} + f_{vol}K_{vol}(\theta_s,\theta_v,\phi_s-\phi_v) + f_{geo}K_{geo}(\theta_s,\theta_v,\phi_s-\phi_v) \quad (1)$$

where $\rho_\lambda(\theta_s, \theta_v, \phi_s - \phi_v)$ is the surface reflectance under specified geometries. f_{iso}, f_{vol}, and f_{geo} are the BRDF kernel model parameters. $K_{vol}(\theta_s, \theta_v, \phi_s - \phi_v)$ is the RossThick model used for its assumption of a dense leaf canopy, and $K_{geo}(\theta_s, \theta_v, \phi_s - \phi_v)$ is the LiSparse kernel used for its assumption of a sparse ensemble of surface objects casting shadows on the background. Once the surface reflectance of the clearest days

for different sensors is given, these surface reflectance values can be employed to estimate the BRDF parameters (f_{iso}, f_{vol}, and f_{geo}). The surface reflectance under cloudy conditions is then calculated using these BRDF parameters at the specified solar and view zenith angles based on Eq. (1). The specific description on how the BRDF parameters are fitted is shown in Appendix I.

3.4. Water vapor correction

Solar irradiances are reduced within the atmosphere. Water vapor absorbs infrared radiation, and the influence of water vapor on the estimation of the surface radiation is significant, especially in the infrared band under cloud-free conditions. The water vapor broadband and spectral transmission parameterization functions have been reported in the literature (Bird & Hulstrom, 1981; Gueymard, 1995; Psiloglou, Santamouris, & Asimakopoulos, 2000; Ryu et al., 2008; Van Laake & Sanchez-Azofeifa, 2004). During the radiative transfer simulations through MODTRAN, the default amount of water vapor was utilized. To reduce the water vapor influences on ISR estimation, a simple normalized water vapor transmittance method was used for the water vapor correction of the solar radiation at the surface. The correction method is applied only to the ISR estimation (not the PAR estimation) because water vapor absorption primarily occurs in the infrared spectrum. The water vapor transmission rate index T_w can be estimated using the following equation (Psiloglou et al., 2000):

$$T_w = 1 - \frac{3.014Mu}{((1+119.3Mu)^{0.644} + 5.814Mu)} \tag{2}$$

where M is the optical atmospheric mass, and u is the water vapor amount in cm. The optical air mass M can be obtained as according to the following equation:

$$M = \left(\cos(\theta_s) + 0.50572(96.07995 - \theta_s)^{-1.6364}\right)^{-1} \tag{3}$$

where θ_s is the solar zenith angle. After the water vapor transmittance is calculated, it is normalized by the following equation:

$$R_w = T_w(u)/T_w(u_d) \tag{4}$$

where R_w is the normalized water vapor transmittance, $T_w(u)$ is the water vapor transmittance at the water vapor amount u in cm, and $T_w(u_d)$ is the water vapor transmittance at the default amount of water vapor. The estimated ISR at the surface is then corrected using the normalized water vapor transmittance R_w.

3.5. Integration procedures

After calculating the ISR and PAR using the improved look-up table algorithm for different sensors, a fusion method is designed to combine the results retrieved from MODIS and the geostationary satellite data to map the ISR and PAR globally. The MODIS data are used to derive the solar radiation at the surfaces that are greater than the north and south latitudes of 60°, and radiation at the lower latitudes is calculated through a combination of polar-orbiting and geostationary satellite-derived radiation products.

Because MODIS observes the surface multiple times at high latitudes, the LUT method, proposed by Wang, Liang, Liu, and Zheng (2010), is used to interpolate for the time that is not observed during the day at high latitudes to fulfill the required 3-hour temporal resolution of this dataset. This method assumes that the atmospheric condition varies only slightly during a given period. The ISR and PAR at high latitudes (higher than the north and south latitudes of 60°) are estimated using the closest time derived from the satellite using the atmospheric index under the same atmospheric condition.

The ISR and PAR at lower latitudes (between the north and south latitudes of 60°) over the land surface are either calculated from the combination of ISR and PAR derived from MODIS data and that derived from the geostationary satellite data or only from the MODIS derived value, because the selected geostationary satellites do not cover all of the land surface at the lower latitudes. The predictive surface solar radiation from different sensors is expressed by the variable r, and the corresponding in-situ measurement at a given time point is r_t. The combination ISR and PAR derived from MODIS data and the geostationary satellite data can be expressed using the following equation:

$$F(\theta_s) = \sum_{r=1}^{R} w_r F_r(\theta_s) \tag{5}$$

where $F(\theta_s)$ and $F_r(\theta_s)$ are the combined ISR and PAR from each sensor and those derived from each sensor, respectively. The weight for each sensor, w_r is given by the determination coefficient of the derived value compared with the ground measurements, which can reflect how well the derived value from each sensor fits the observed data and is assumed to have a Gaussian distribution.

4. Generating GLASS solar radiation products

4.1. GLASS products

The algorithms and procedures described above have been implemented to generate the global ISR and PAR products using the Global LAnd Surface Satellite (GLASS) production system (Zhao et al., 2013). The GLASS ISR and PAR products are generated through three main procedures. First, The MODIS L1B data are converted into a sinusoidal projection and the surface reflectance is estimated using the described method for both MODIS and the geostationary satellite data. Then, the ISR and PAR are approximated using the estimated surface reflectance based on the two created look-up tables for the visible band of each sensor. Finally, the global ISR and PAR are generated with 5 km spatial resolution and 3 hour temporal resolution through the combination of ISR and PAR from both MODIS and geostationary satellite data. The quality of the generated ISR and PAR products were primarily dependent on the sky conditions, snow cover, and surface reflectance. Thus, the quality of these two products is indicated by a scientific dataset, which includes information on the cloud state, cloud shadow, surface reflectance quality, and snow cover within a 16-bit unsigned integer.

In this study, both ISR and PAR products for each sensor and global products from all of the selected satellites are generated. The respective spatial and temporal resolutions are 5 km and 3 h for GOES11 and GOES12, 5 km and 1 h for MTSAT, and 5 km and 15 min for MSG2, as illustrated in Figs. 9–12. We can obtain the global ISR and PAR products using only the MODIS data, but certain gaps remain in the derived images, which is one of the reasons that we utilize both polar-orbiting and geostationary satellite data to generate the global ISR and PAR products, as illustrated in Fig. 13. The global instantaneous fusion products of the ISR are shown in Fig. 14, which is provided in a gridded equal-angle projection with a 5 km spatial resolution and a 3 hour temporal resolution. The MODIS derived global ISR and that derived from multiple satellite data have a similar spatial pattern as shown in Figs. 13 and 14. Because the satellite imagery is a snapshot of the Earth, the direct estimation of solar radiation from the imagery is typically the instantaneous value. The temporally integrated solar radiation is more significant for climatic and ecological applications. Thus, we also generate the daily integrated ISR and PAR using a sinusoidal interpolation method to predict the daily PAR from instantaneous values. The daily integrated global PAR products estimated from the instantaneous PAR values are shown in Fig. 15, which have larger values in the northern hemisphere and smaller values in the southern hemisphere due to the daytime is long in the northern hemisphere and generally increases as latitude

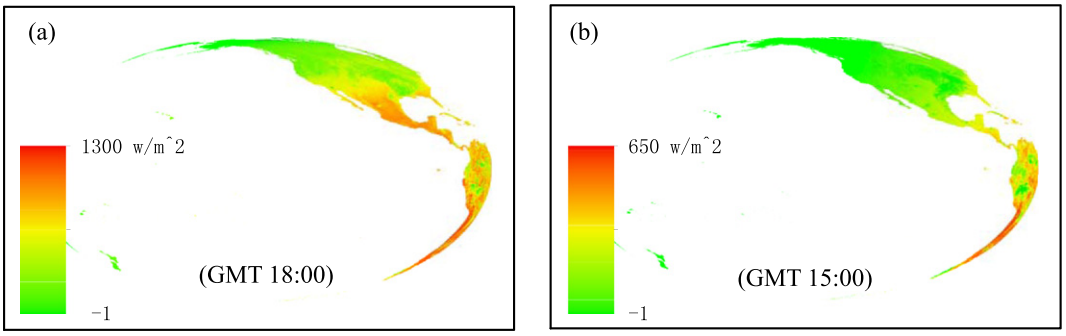

Fig. 9. The retrieved ISR (a) and PAR (b) using GOES12 data at 14:45 (GMT) and 17:45 (GMT) on November 12, 2008.

increases in the summer. The generated ISR and PAR products will be available publicly from the Beijing Normal University Data Center for Global Change Data Processing and Analysis (http://www.bnu-datacenter.com/) and the global land cover facility from the University of Maryland (http://glcf.umd.edu/).

4.2. Validation with ground measurements

Because the ground measurements from the selected radiation network are collected at different time frequencies (2, 3, and 30 min), the GLASS ISR and PAR products are compared with the 30 min average of the measured ISR and PAR to reduce the possible mismatch of space and time at these selected sites. To be consistent, it was assumed that the radiation components maintain the same value for a period of time (here for 30 min). The instantaneous estimates of ISR and PAR at the surface were compared with the ground measurements at the time closest to the instantaneous retrieved values during the entire year at SURFRAD, AmeriFlux, CarbonEuropeIP, AERONET, and Asia flux sites and during the summer season (July, August, and September) at the COIRAS sites in 2008.

The accuracy was assessed by means of two widely used statistical estimators [root mean square error (RMSE), and mean bias error (BIAS)]. The validation results summarized in Table 4 demonstrate that the GLASS ISR and PAR products are accurate under all sky conditions. The overall coefficient of determination at these sites is 0.83 and 0.84 for ISR and PAR, respectively. The bias values for ISP and PAR are -6.5 Wm^{-2} and 5.0 Wm^{-2}, respectively, and the RMSE values are 115.0 Wm^{-2} and 49.0 Wm^{-2}, respectively. As shown in Table 4, the validation results at the SURFRAD sites are better than those at other sites except the Desert Rock site, which may be due to the time scales released by the data centers. The SURFRAD sites released the measurements every 3 min and are always believed to have better quality; however, a 30 minute average was used for the CarbonEuropeIP and COIIRAS sites. The validation results at the Desert Rock site show the maximum RMSE of -55 Wm^{-2}. To obtain more insight in to these discrepancies at this site, we further investigate the details of this site. The Desert Rock (36.63°N, 116.02°W) site at SURFRAD, which is located 65 miles northwest of Las Vegas, has an elevation higher than 1000 m. The Desert Rock land surface is covered by fine rock and scattered desert shrubs. We conclude that the systematic errors are primarily due to the climatic conditions, the altitude, and the absolute accuracy of the pyrometer at the Desert Rock site. The absolute accuracy of pyrometers has never been better than 5% or 10 Wm^{-2} (Dutton, 1993).

Elevation is one of the important factors controlling the accuracy of radiation retrieval at the surface using satellite observations. Yang et al. (2008, 2010) pointed out that the accuracy of the satellite shortwave radiation products was typically greater in highly variable terrain and less in non-variable terrain and the GEWEX-SRB (V2.5) dataset much underestimated ISR over the Tibet Plateau. The underestimation is caused by the discrepant input data among individual satellite products over high altitude regions. As shown in Table 4, the validation results of GLASS ISR and PAR products have larger discrepancies at high altitude sites (>1000 m), but a lower bias at low latitude sites, which is consistent with the conclusions by Yang et al. (2008, 2010). The COIRAS Arou site (38.04°N, 100.46°E), which is located on the Tibet Plateau, is a freeze–thaw meteorological observation site located 3032 m above sea level in the Qinghai Province in China. The land surface at this site is covered by 20–30 cm high grasses in the summer. The surface in this region is frozen from the end of October to May of the following year. The comparison of the instantaneous GLASS ISR product with ground measurements shows an average bias of -23 Wm^{-2} and a RMSE of 119 Wm^{-2}, which indicates that the GLASS ISR product is likely to perform better than other satellite radiation products (Gui et al., 2010; Yang et al., 2010, 2008). Although the surface elevation is considered during the radiative transfer simulation for generating GLASS ISR and PAR products, the atmospheric profile will be altered if the elevation varies, which will cause errors to obtain the water vapor amount and will ultimately influence the water vapor correction. Thus, we conclude that the elevation and the atmospheric profile influences on ISR and PAR estimation should be further investigated, and that this estimation will be improved in the next version of the GLASS products.

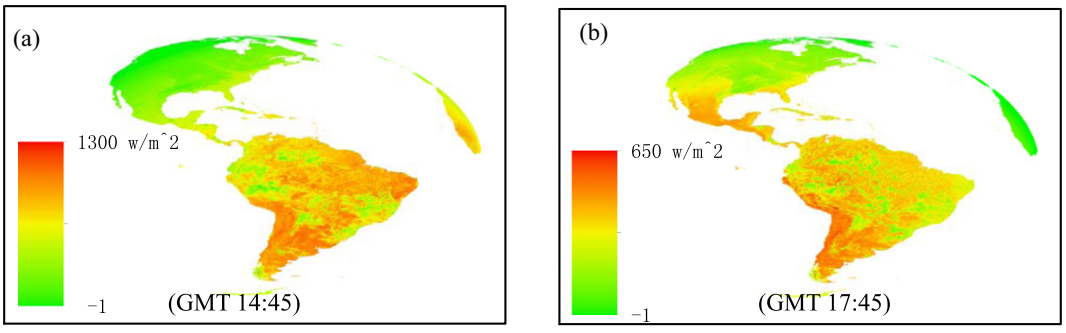

Fig. 10. The retrieved ISR (a) and PAR (b) using GOES12 data at 14:45 (GMT) and 17:45 (GMT) on November 12, 2008.

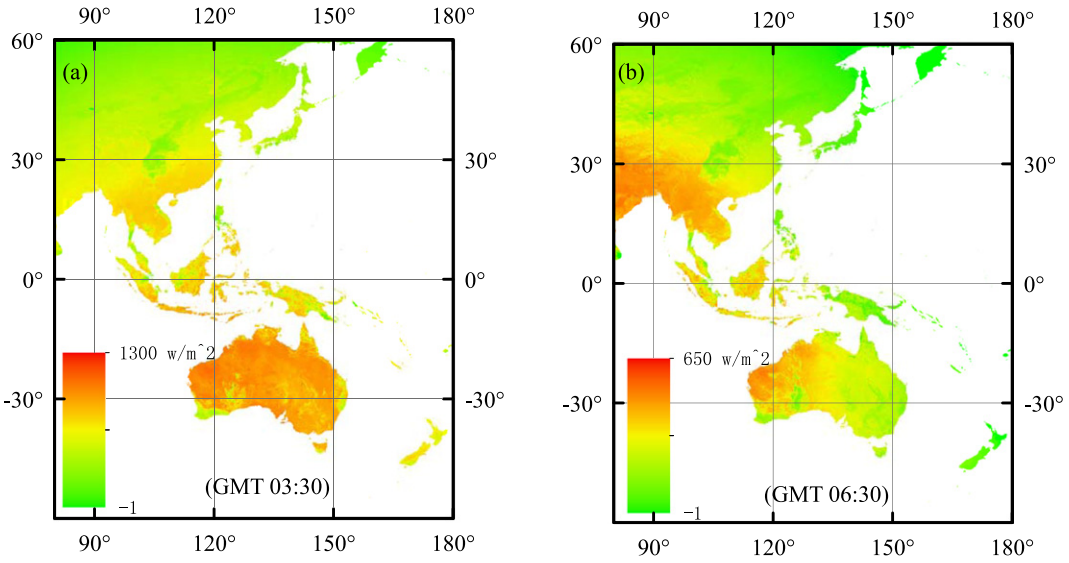

Fig. 11. The retrieved ISR (a) and PAR (b) using MTSAT data at 03:30 (GMT) and 06:30 (GMT) on November 12, 2008.

A comparison of the GLASS ISR products with the ground measurements at the COIRAS sites demonstrates that the GLASS ISR is estimated with an average determination coefficient of 0.84, but with a higher than average bias of −13 Wm^{-2}. We conclude that the lager discrepancies at the COIRAS sites are caused by the mismatch in the time between the satellite and ground measurements (released every 30 min on average), and the high elevation at these sites (mean altitudes greater than 1500 m). In addition to these two factors, the climatic condition may also cause errors in ISR and PAR estimation. The COIRAS sites are located in the arid and semi-arid regions of China. In addition, the slight underestimation of the surface solar irradiance by GLASS ISR and PAR products could be caused by inappropriate assumptions about aerosol information (rural) and pollution from certain sites. The small magnitude of bias indicates that the overall systematic deviation is negligible.

The MODIS water vapor amount product is used as input data for the consideration of water vapor correction for ISR estimation. Although the MODIS water vapor amount product is provided every day, many gaps remain between swaths, which will also cause errors and strips in generating the global ISR product. The water vapor dataset will be replaced with other products with higher spatial and temporal resolutions. The GLASS instantaneous ISR and PAR products are reasonably accurate with an average bias of −6.5 Wm^{-2} and −5 Wm^{-2}, respectively.

4.3. Comparison with other products

A major objective of the World Climate Research Programme (WCRP) and numerous national programs (IPCC, 2007) has been to obtain accurate estimates of the radiation budget at the global scale. Currently, the radiation budget component data are available from numeric models, reanalysis data and from satellite observations. It is possible to present an assessment of current available estimates as more information becomes available. To better assess the quality of the GLASS ISR product and to give a comparison with other data, we compare the GLASS ISR to results from ISCCP-FD and CERES at 7 SURFRAD sites in 2008. The ISCCP-FD estimates the ISR using a NASA Goddard Institute for Space Studies (GISS) radiative transfer model with improved observations of the physical properties of the surface, atmosphere, and clouds based on the ISCCP data sets at approximately a 280 km spatial resolution and a 3-hour temporal resolution from 1983 to 2009 (Zhang et al., 1995, 2004).

The CERES ISR product is derived using different models (Model A, Model B, Model C, and the CALISPO, CERES, Clousat and MODIS (CCCM) enhanced products). Models A and C are excluded in this study because only a few of the retrieved results are valid in this product version in 2008. The CERES surface shortwave Model B depends on

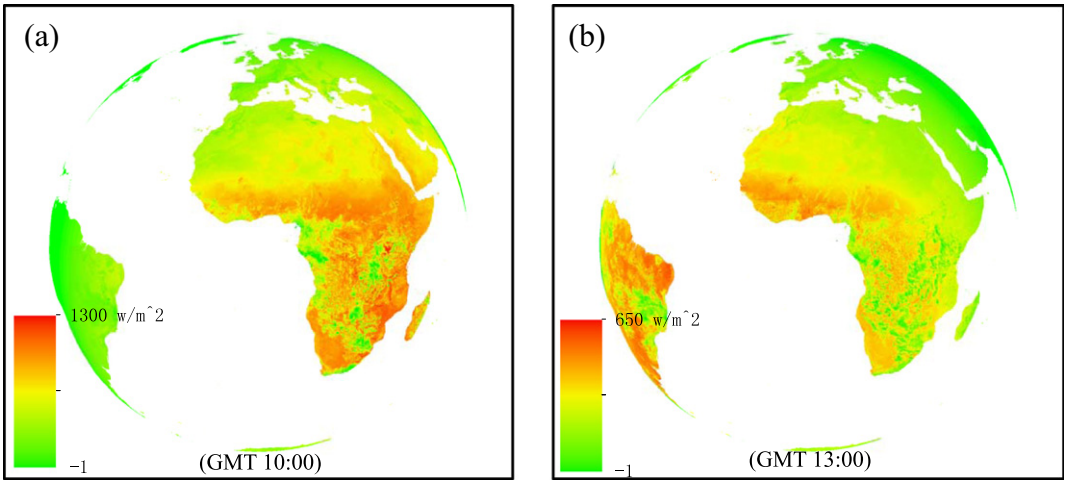

Fig. 12. The retrieved ISR (a) and PAR (b) using MSG2 data at 10:00 (GMT) and 13:00 (GMT) on November 12, 2008.

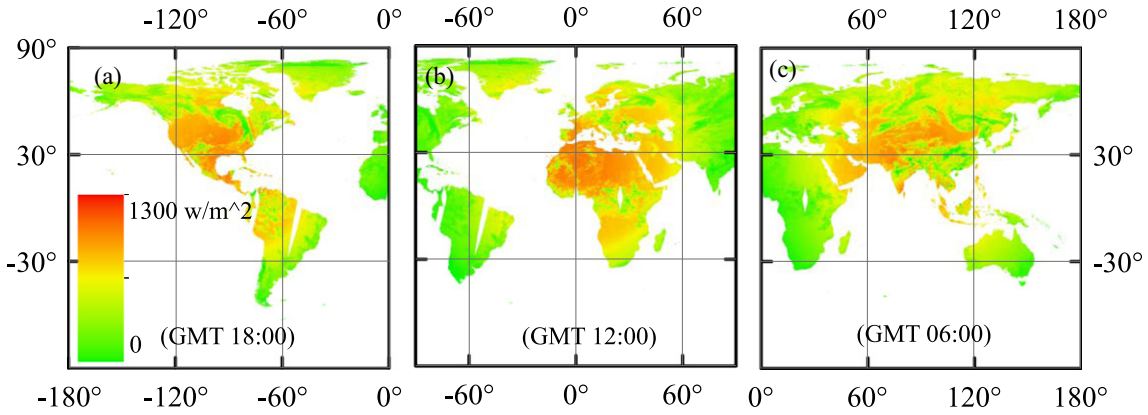

Fig. 13. The estimated global instantaneous ISR based on MODIS observations on June 27, 2008.

simple relationships to estimate the attenuation of the surface insolation by the Earth's atmosphere for both clear- and cloudy-sky conditions (Gupta, Kratz, Stackhouse, & Wilber, 2001). The CCCM enhanced product is derived from a two-step process. First, three 333 m resolution CALIPSO profiles of one 1.4 km Cloudsat profile are collocated with each 1 km MODIS imager pixel using geolocation information. Then, these 1 km data are collocated with 20 km CERES footprints. Subsequently, we aggregated the spatial resolutions of the GLASS insolation product to match the ISCCP-FD and CERES, and the validation results are shown in Table 5. The GLASS product is more accurate than these two products at these validation sites, but all of these three datasets have a low precision at the Desert Rock site.

We also compare the latitudinal pattern of the GLASS ISR product with ISCCP-FD ISR product to give a comprehensive comparison between these two products. To perform the comparison, we generate the daily integrated ISR using the sinusoidal interpolation method to predict the daily integrated ISR from the ISCCP-FD 3 hourly values. Then, the daily integrated ISR of both GLASS and ISCCP-FD products is used to calculate the monthly and annual mean product to perform the comparison. The zonal mean of ISCCP-FD ISR product is calculated by the area weighted averaging in the latitudinal zone, because the ISCCP-FD ISR product is provided in gridded equal-angle projection. We also aggregated the spatial resolutions of the GLASS insolation product to match the ISCCP. Fig. 16 shows the latitudinal pattern of the estimated annual mean GLASS ISR compared to that of ISCCP-FD ISR product in 2009. It is obvious that the GLASS ISR product has similar latitudinal pattern to the ISCCP-FD data.

5. Conclusions and discussion

High-resolution ISR and PAR data are required for many land applications. However, the existing global products have coarse spatial resolutions. In particular, long-term series of coarse-resolution PAR data are not routinely available. PAR is typically obtained by multiplying the ISR by a constant. In this study, we present a practical scheme to generate the GLASS ISR and PAR products based on the LUT method from MODIS and multiple geostationary satellite data. The look-up table method primarily considers the influences of surface elevation, atmospheric water vapor, and a surface bi-directional reflectance distribution function (BRDF) on ISR and PAR estimation. The GLASS ISR and PAR products are provided with a 5 km spatial resolution and a 3-hour temporal resolution from 2008 to 2010.

The validation results of the GLASS ISR and PAR at 34 sites from different ground measurements are very promising. The overall coefficient of determination at these sites is 0.83 and 0.84 for ISR and PAR, respectively. The bias is -6.5 Wm^{-2} and 5.0 Wm^{-2}, and the RMSE is 115.0 Wm^{-2} and 49.0 Wm^{-2} for ISR and PAR, respectively. Similar to other global radiation products, the validation results show that the retrieved ISR and PAR have larger discrepancies at high altitude sites but smaller discrepancies at low altitude sites.

The sensitivity analyses presented in this study demonstrate that ISR and PAR estimation is insensitive to the atmospheric profiles and the ozone amount. The water vapor amount has a very strong absorption on ISR but very weak effects on PAR at the surface. The surface elevation may cause an error of up to 100 Wm^{-2} and is a significant source of

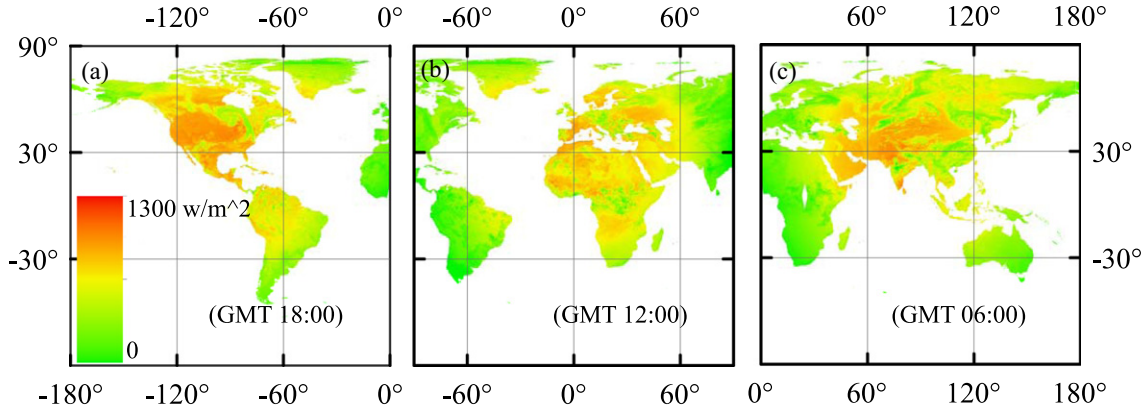

Fig. 14. The estimated global instantaneous ISR product using data from multiple polar-orbiting and geostationary satellites on June 27, 2008.

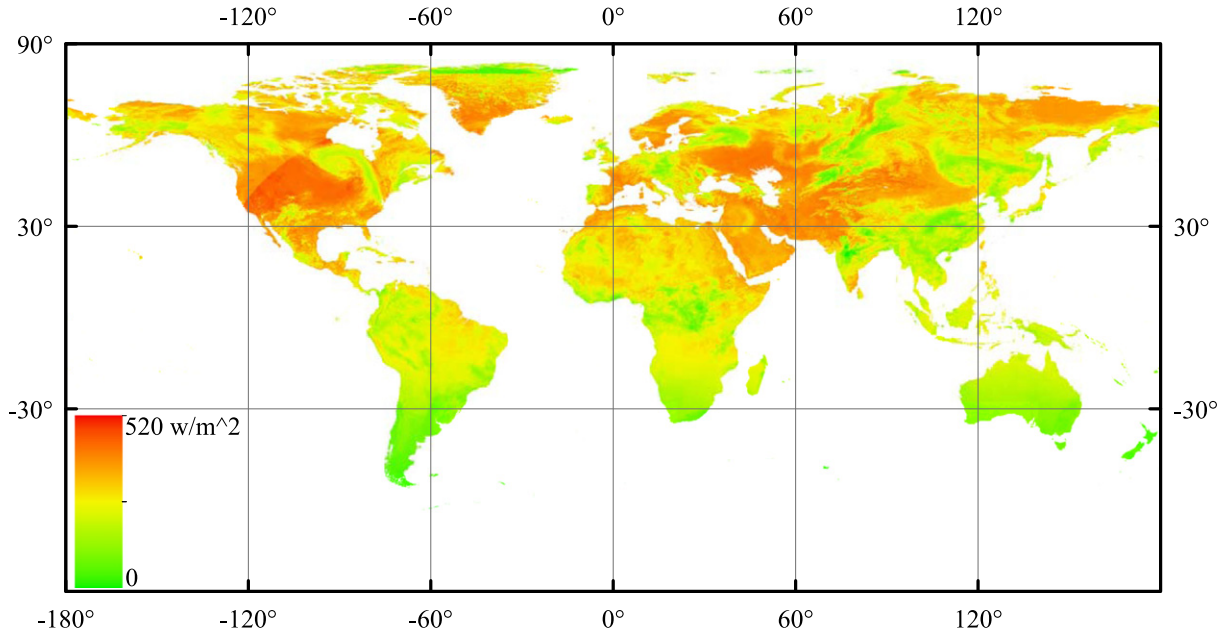

Fig. 15. The integrated daily PAR from the instantaneous GLASS PAR products on June 27, 2008.

error in ISR and PAR estimation. The ISR and PAR estimation is more sensitive to the aerosol modes, especially the urban aerosol type, which is not considered in this study. The estimation of ISR and PAR may be significantly improved by using better aerosol information (aerosol types and size distributions) and, especially, a better elevation correction method and atmospheric profiles.

In addition to the accuracy of the retrieval algorithm, the accuracy of the ground measurements, the quality of the input parameters, and the instrument calibration errors, the validation of satellite retrieved radiation components, including ISR and PAR, is also dependent on the spatial representativeness of ground measurements and the time difference between the remote sensing and ground measurements. In this study, we directly compare the retrieved instantaneous ISR and PAR with ground measurements within 30 min on average at all of the selected sites, which may also be one of the source errors at these sites.

The GLASS ISR and PAR values are not divided into direct and diffuse components. Generally, the diffuse components of the ISR and PAR are essential to many applications. Therefore, the direct and diffuse values should be provided and validated in the future. Moreover, although three years of ISR and PAR values are generated, these data remain insufficient for use with long-term radiation budget analyses and other applications. Efforts are underway to produce long-term series.

Table 4
A summary of the statistics of the comparison of the ground measurements and the estimated instantaneous ISR and PAR from multiple satellite data at the 34 selected sites.

Site	ISR			PAR		
	R^2	BIAS	RMSE	R^2	BIAS	RMSE
Bondville	0.86	20	100	0.86	4.6	45
FortPeck	0.82	5.5	111	0.82	1.6	46
Goodwin Creek	0.92	1.7	86	0.91	4.2	38
Penn State	0.87	12	100	0.86	9.4	44
Sioux Falls	0.86	14	102	0.86	2.4	43
Boulder	0.77	−8.7	140	0.78	−7.6	58
Desert Rock	0.88	−55	119	0.89	−30	51
ARM-SGP Main	0.9	−7.73	93	0.88	16	45
Audubon Research Ranch	0.86	−42	120	0.87	24	56
Brookings	0.83	−9	114	0.84	33	55
Fermi_Agricultural	0.77	55	145	0.78	2	61
Flagstaff Managed Forest	0.78	−26	150	0.77	−19	68
Flagstaff UnManaged Forest	0.86	−24	110	0.88	−4	44
Neustift	0.8	−48	140	0.83	−5	48
Lonzee	0.6	2	131	0.74	9	48
Vielsalm	0.75	12	107	0.79	22	47
Laegeren	0.77	−41	146	0.83	−4	49
Oensingen2 crop	0.77	−10	129	0.86	−9	47
Bily Kriz-Beskidy Mountains	0.77	17	121	0.83	24	48
Bily Kriz grassland	0.79	−3	119	0.82	25	49
CZECHWET	0.88	−17	84	0.86	11	41
Moldova	0.89	34	97	0.85	7	47
Alta_Floresta	0.87	2	108	/		
CEILAP-BA	0.82	−23	123			
Kherlenbayan Ulaan	0.9	31	94			
Arou	0.83	−23	119			
Changwu	0.82	24	111			
Dayekou	0.84	−20	133			
Dingxi	0.85	16	101			
Dongsu	0.85	−44	115	0.82	−5	48
Tongyu	0.81	−8	106	/		
Yingke	0.85	−31	117			
Yuzhong	0.8	−22	131			
Zhangye	0.87	−6	93			
Total	0.83	−6.5	115	0.84	5	49

Acknowledgments

We thank the SURFRAD, AmeriFlux, AERONET, CarbonEuropeIP, AsiaFlux, and COIRAS programs as well as the principal investigators of the selected sites at which the ground measurement data were provided for our validation. We would also like to thank NASA/EOS for providing the MODIS data, NOAA for the GOES data, EUMESAT for the MSG SEVIRI data, and JMA for the MTSAT data. This work was supported by grants from the National High Technology Research and Development Program of China (863 program) (no. 2013AA122800 and no. 2009AA122103), the Natural Science Foundation of China (no. 41101310 and no. 4133 1173), the Fundamental Research Funds for the Central universities (no. 2013YB38), and the International S&T Cooperation Program of China (no. 2012DFG21710). The GLASS products are available from the Beijing Normal University Data Center for Global Change Data Processing and Analysis (http://www.bnu-datacenter.com/) and the Global Land Cover Facility from the University of Maryland (http://glcf.umd.edu/).

Table 5
Comparison of the retrieved three-hour GLASS ISR product, the International Satellite Cloud Climatology Project — Flux Data (ISCCP-FD), the CERES Model B, and the CALISPO, CERES, Clousat and MODIS (CCCM) enhanced products in 2008.

Site	GLASS ISR			ISCCP-FD			CERES					
							Model B			CCCM enhanced		
	R^2	Bias	RMSE	R^2	Bias	RMSE	R^2	Bias	RMSE	R^2	Bias	RMSE
Bondville	0.87	14.68	104.97	0.71	−7.06	149.88	0.84	12.9	119.5	0.82	−0.5	126.16
FortPeck	0.84	10.51	102.75	0.69	9.61	150.37	0.81	5.3	112.40	0.80	2.3	115.02
Goodwin Creek	0.91	−6.29	99.54	0.64	12.61	184.11	0.69	14.3	172.0	0.66	−3.8	179.35
Penn State	0.85	18.17	109.3	0.7	5.92	152.88	0.87	6.9	107.0	0.86	−8.6	111.18
Sioux Falls	0.81	11.52	114.41	0.65	37.83	168.85	0.62	−11.4	167.4	0.58	−37.8	178.77
Boulder	0.81	−12.8	126.38	0.72	6.49	154.96	0.34	−12.0	249.3	0.47	−43.0	214.41
Desert Rock	0.92	−52.4	112.94	0.87	−42.4	125.27	0.52	−24.2	198.0	0.49	−26.6	206.38

Appendix I

The percentages of 15 of the total observations are identified as the clearest observations within the temporal window. These lowest 15% surface reflectances, derived for the "clearest" observations, are regarded as the actual surface reflectance to fit the RossThcik-LiSparse model to characterize the surface bidirectional feature. The RossThcik-LiSparse model is a weighted function of the isotropic parameter and two kernels of viewing and illumination geometry. The weighted function is presented in Eq. (1) (Lucht et al., 2000). RossThick kernel, $K_{vol}(\theta_s, \theta_v, \phi_s - \phi_v)$, and LiSparse kernel, $K_{geo}(\theta_s, \theta_v, \phi_s - \phi_v)$, can be derived using the following equations:

$$K_{vol}(\theta_s,\theta_v,\phi_s-\phi_v)=\frac{(\pi/2-\xi)\cos\xi+\sin\xi}{\cos\theta_s+\cos\theta_v}-\pi/4 \tag{A1}$$

$$K_{geo}(\theta_s,\theta_v,\phi_s-\phi_v)=O(\theta_s,\theta_v,\phi_s-\phi_v)-\sec\theta_s'-\sec\theta_v'+\frac{1}{2}(1+\cos\xi')\sec\theta_s'\sec\theta_v' \tag{A2}$$

$$\cos\xi=\cos\theta_s\cos\theta_v+\sin\theta_s\sin\theta_v\cos(\phi) \tag{A3}$$

$$O(\theta_s,\theta_v,\phi_s-\phi_v)=\frac{1}{\pi}(t-\sin t\cos t)(\sec\theta_s'+\sec\theta_v') \tag{A4}$$

$$\cos t=\frac{h}{b}\sqrt{\frac{D^2+(\tan\theta_s'\tan\theta_v'\sin\phi)^2}{\sec\theta_s'+\sec\theta_v'}} \tag{A5}$$

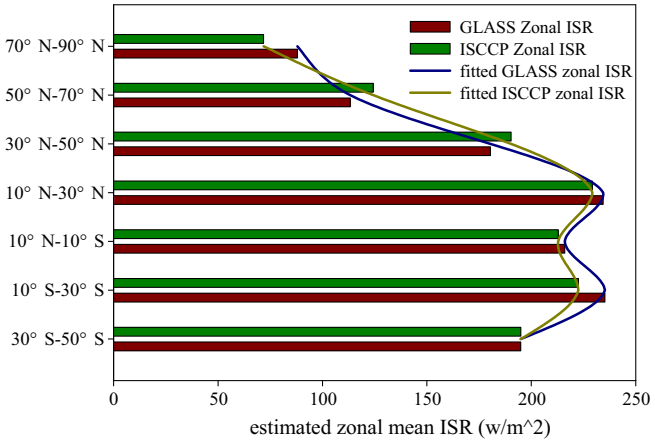

Fig. 16. Comparison of the latitudinal pattern of the GLASS and ISCCP-FD ISR products.

$$D=\sqrt{\tan^2\theta_s'+\tan^2\theta_v'-2\tan\theta_s'\tan\theta_v'\cos\phi} \tag{A6}$$

$$\cos\xi'=\cos\theta_s'\cos\theta_v'+\sin\theta_s'\sin\theta_v'\cos(\phi)' \tag{A7}$$

$$\theta_s'=\tan^{-1}\left(\frac{b}{r}\tan\theta_s\right)\ \text{and}\ \theta_v'=\tan^{-1}\left(\frac{b}{r}\tan\theta_v\right) \tag{A8}$$

where θ_s, θ_v, and ξ are the solar zenith angle, view zenith angle, and the phase angle, respectively. $O(\theta_s, \theta_v, \phi_s - \phi_v)$ is the area of overlap between the view and solar shadows, and h/b and b/r are the crown shape parameters, which are equal to 2 and 1, respectively. After the surface reflectance of the clearest days for different sensors is obtained based on the LUT, these surface reflectance values can be employed to estimate the BRDF parameters (f_{iso}, f_{vol}, and f_{geo}) through the least-square estimation. The surface reflectance under "hazy/cloudy" conditions is then calculated using these BRDF parameters at the specified solar and view zenith angles based on Eq. (1).

References

Anderson, G. P., Berk, A., Acharya, P. K., Matthew, M. W., Bernstein, L. S., James, H., et al. (1999). MODTRAN4: Radiative transfer modeling for remote sensing. In K. Anton, & D. G. John (Eds.), SPIE.

Angstrom, A. (1924). Solar and terrestrial radiation. Report to the international commission for solar research on actinometric investigations of solar and atmospheric radiation. *Quarterly Journal of the Royal Meteorological Society, 50*, 121–126.

Augustine, J. A., Deluisi, J., & Long, C. N. (2000). SURFRAD—A national surface radiation budget network for atmospheric research. *Bulletin of the American Meteorological Society, 81*, 2341–2357.

Augustine, J. A., Hodges, G. B., Cornwall, C. R., Michalsky, J. J., & Medina, C. I. (2005). An update on SURFRAD—The GCOS surface radiation budget network for the Continental United States. *Journal of Atmospheric and Oceanic Technology, 22*, 1460–1472.

Baldocchi, D., Falge, E., Gu, L., Olson, R., Hollinger, D., Running, S., et al. (2001). FLUXNET: A new tool to study the temporal and spatial variability of ecosystem-scale carbon dioxide, water vapor, and energy flux densities. *Bulletin of the American Meteorological Society, 82*, 2415–2434.

Bird, R. E., & Hulstrom, R. L. (1981). A simplified clear sky model for direct and diffuse insolation on horizontal surfaces. *Technical report no. SERI/TR-642-761* (Golden, Colorado).

Cano, D., Monget, J. M., Albuisson, M., Guillard, H., Regas, N., & Wald, L. (1986). A method for the determination of the global solar radiation from meteorological satellite data. *Solar Energy, 37*, 31–39.

Dubayah, R. (1992). Estimating net solar radiation using Landsat Thematic Mapper and digital elevation data. *Water Resources Research, 28*, 2469–2484.

Dutton, E. G. (1993). An extended comparison between LOWTRAN7 computed and observed broadband thermal irradiances: Global extreme and intermediate surface conditions. *Journal of Atmospheric and Oceanic Technology, 10*, 326–336.

Frouin, R., & McPherson, J. (2012). Estimating photosynthetically available radiation at the ocean surface from GOCI data. *Ocean Science Journal, 47*, 313–321.

Frouin, R., McPherson, J., Ueyoshi, K., & Franz, B. A. (2012). A time series of photosynthetically available radiation at the ocean surface from SeaWiFS and MODIS data. *Proc. SPIE 8525, Remote Sensing of the Marine Environment II, 852519.*

Gautier, C., Diak, G., & Masse, S. (1980). A simple physical model to estimate incident solar radiation at the surface from GOES satellite data. *Journal of Applied Meteorology, 19*, 1005–1012.

Gilgen, H., & Ohmura, A. (1999). The global energy balance archive. *Bulletin of the American Meteorological Society*, *80*, 831–850.
Gueymard, C. (1995). *SMARTS2, A Simple Model of Atmospheric Radiative Transfer of Sunshine: Algorithms and performance assessment*. Cocoa, FL: Florida Solar Energy Center.
Gui, S., Liang, S., Wang, K., Li, L., & Zhang, X. (2010). Assessment of three satellite-estimated land surface downwelling shortwave irradiance data sets. *IEEE Geoscience and Remote Sensing Letters*, *77*, 776–780.
Gupta, S. K., Kratz, D. P., Stackhouse, P. W., & Wilber, A. C. (2001). *The Langley Parameterized Shortwave Algorithm (LPSA) for surface radiation budget studies, NASA TP-2001-211272*. (31 pp.).
Harries, J. E., Russell, J. E., Hanafin, J. A., Brindley, H., Futyan, J., Rufus, J., et al. (2005). The geostationary Earth Radiation Budget Project. *Bulletin of the American Meteorological Society*, *86*, 945–960.
Hubanks, P. A., King, M.D., Platnick, S., & Pincus, R. (2006). *The MODIS atmosphere L3 grided product*. Algorithm Theoretical Basis Document.
IPCC (2007). *Climate change 2007: The physical science basis: Working group I contribution to the Fourth Assessment Report of the IPCC. New York*.
Laszlo, I., Ciren, P., Liu, H. Q., Kondragunta, S., Tarpley, J.D., & Goldberg, M.D. (2008). Remote sensing of aerosol and radiation from geostationary satellites. *Advances in Space Research*, *41*, 1882–1893.
Liang, S., Wang, K., Zhang, X., & Wild, M. (2010). Review on estimation of land surface radiation and energy budgets from ground measurement, remote sensing and model simulations. *IEEE Journal of Selected Topics in Applied Earth Observations and Remote Sensing*, *3*, 225–240.
Liang, S., Zhao, X., Liu, S., Yuan, W., Cheng, X., Xiao, Z., et al. (2013). A long-term Global LAnd Surface Satellite (GLASS) data-set for environmental studies. *International Journal of Digital Earth*, *6*(Suppl. 1), 6–33.
Liang, S., Zheng, T., Liu, R., Fang, H., Tsay, S.C., & Running, S. (2006). Estimation of incident photosynthetically active radiation from Moderate Resolution Imaging Spectrometer data. *Journal of Geophysical Research, Atmospheres*, *111*, D15208.
Liang, S., Zheng, T., Wang, D., Wang, K., Liu, R., Tsay, S. -c., et al. (2007). Mapping high-resolution incident photosynthetically active radiation over land from polar-orbiting and geostationary satellite data. *Photogrammetric Engineering and Remote Sensing*, *73*, 1085–1089.
Liu, R., Liang, S., He, H., Liu, J., & Zheng, T. (2008). Mapping incident photosynthetically active radiation from MODIS data over China. *Remote Sensing of Environment*, *112*, 998–1009.
Liu, X., Mei, X., Li, Y., Zhang, Y., Wang, Q., Jensen, J. R., et al. (2009). Calibration of the Ångström–Prescott coefficients (a, b) under different time scales and their impacts in estimating global solar radiation in the Yellow River basin. *Agricultural and Forest Meteorology*, *149*, 697–710.
Lu, N., Liu, R., Liu, J., & Liang, S. (2010). An algorithm for estimating downward shortwave radiation from GMS 5 visible imagery and its evaluation over China. *Journal of Geophysical Research, Atmospheres*, *115*, D18102.
Lucht, W., Schaaf, C. B., & Strahler, A. H. (2000). An algorithm for the retrieval of albedo from space using semiempirical BRDF models. *IEEE Transactions on Geoscience and Remote Sensing*, *38*, 977–998.
Meza, F., & Varas, E. (2000). Estimation of mean monthly solar global radiation as a function of temperature. *Agricultural and Forest Meteorology*, *100*, 231–241.
Mueller, R. W., Matsoukas, C., Gratzki, A., Behr, H. D., & Hollmann, R. (2009). The CM-SAF operational scheme for the satellite based retrieval of solar surface irradiance — A LUT based eigenvector hybrid approach. *Remote Sensing of Environment*, *113*, 1012–1024.
Muneer, T., Younes, S., & Munawwar, S. (2007). Discourses on solar radiation modeling. *Renewable and Sustainable Energy Reviews*, *11*, 551–602.
Ohmura, A., Dutton, E. G., FORGAN, B., Fröhlich, C., Gilgen, H., Hegner, H., et al. (1998). Baseline Surface Radiation Network (BSRN/WCRP): New precision radiometry for Climate Research. *Bulletin of the American Meteorological Society*, *79*, 2115–2136.
Olofsson, P., Van Laake, P. E., & Eklundh, L. (2007). Estimation of absorbed PAR across Scandinavia from satellite measurements: Part I: Incident PAR. *Remote Sensing of Environment*, *110*, 252–261.
Otkin, J. A., Anderson, M. C., Mecikalski, J. R., & Diak, G. R. (2005). Validation of GOES-based insolation estimates using data from the U.S. Climate Reference Network. *Journal of Hydrometeorology*, *6*, 460–475.
Paulescu, M., & Schlett, Z. (2003). A simplified but accurate spectral solar irradiance model. *Theoretical and Applied Climatology*, *75*, 203–212.
Pinker, R. T., & Laszlo, I. (1992). Modeling surface solar irradiance for satellite applications on a global scale. *Journal of Applied Meteorology*, *31*, 194–211.
Psiloglou, B. E., & Kambezidis, H. D. (2007). Performance of the meteorological radiation model during the solar eclipse of 29 March 2006. *Atmospheric Chemistry and Physics*, *7*, 6047–6059.
Psiloglou, B. E., Santamouris, M., & Asimakopoulos, D. N. (2000). Atmospheric broadband model for computation of solar radiation at the Earth's surface. Application to Mediterranean climate. *Pure and Applied Geophysics*, *157*, 829–860.
Qin, J., Yang, K., Liang, S., & Tang, W. (2011). Estimation of daily mean photosynthetically active radiation under all-sky conditions based on relative sunshine data. *Journal of Applied Meteorology and Climatology*, *51*, 150–160.
Running, S. W., Nemani, R., Glassy, J. M., & Thornton, P. E. (1999). *Modis Daily Photosynthesis (PSN) and annual Net Primary Production (NPP) product (MOD17)*. Algorithm Theoretical Basis Document. Version 3.0.
Running, S. W., Thornton, P. E., Nemani, R., & Glassy, J. M. (2000). Global terrestrial gross and net primary productivity from the earth observing system. *Methods in Ecosystem Science*, 44–57.
Ryu, Y., Kang, S., Moon, S. K., & Kim, J. (2008). Evaluation of land surface radiation balance derived from Moderate Resolution Imaging Spectroradiometer (MODIS) over complex terrain and heterogeneous landscape on clear sky days. *Agricultural and Forest Meteorology*, *148*, 1538–1552.
Shahi, N. R., Agarwal, N., Sharma, R., Thapliyal, P. K., Joshi, P. C., & Sarkar, A. (2010). Improved estimation of shortwave radiation over equatorial Indian Ocean using geostationary satellite data. *IEEE Geoscience and Remote Sensing Letters*, *7*, 563–566.
Tang, H., Yu, K., Hagolle, O., Jiang, K., Geng, X., & Zhao, Y. (2013). A cloud detection method based on a time series of MODIS surface reflectance images. *International Journal of Digital Earth*, 1–15.
Van Laake, P. E., & Sanchez-Azofeifa, G. A. (2004). Simplified atmospheric radiative transfer modelling for estimating incident PAR using MODIS atmosphere products. *Remote Sensing of Environment*, *91*, 98–113.
Vermote, E. F., Saleous, N. Z. E., & Justice, C. O. (2002). Atmospheric correction of MODIS data in the visible to middle infrared: First results. *Remote Sensing of Environment*, *83*, 97–111.
Wang, K., Dickinson, R. E., Wild, M., & Liang, S. (2010a). Evidence for decadal variation in global terrestrial evapotranspiration between 1982 and 2002: 1. Model development. *Journal of Geophysical Research, Atmospheres*, *115*, D20112.
Wang, K., Dickinson, R. E., Wild, M., & Liang, S. (2010b). Evidence for decadal variation in global terrestrial evapotranspiration between 1982 and 2002: 2. Results. *Journal of Geophysical Research, Atmospheres*, *115*, D20113.
Wang, D., Liang, S., Liu, R., & Zheng, T. (2010). Estimation of daily-integrated PAR from sparse satellite observations: Comparison of temporal scaling methods. *International Journal of Remote Sensing*, *31*, 1661–1677.
Wang, K., Zhou, X., Liu, J., & Sparrow, M. (2005). Estimating surface solar radiation over complex terrain using moderate-resolution satellite sensor data. *International Journal of Remote Sensing*, *26*, 47–58.
Wu, H., Zhang, X., Liang, S., Yang, H., & Zhou, G. (2012). Estimation of clear-sky land surface longwave radiation from MODIS data products by merging multiple models. *Journal of Geophysical Research, Atmospheres*, *117*, D22107.
Yang, K., He, J., Tang, W., Qin, J., & Cheng, C. C. K. (2010). On downward shortwave and longwave radiations over high altitude regions: Observation and modeling in the Tibetan Plateau. *Agricultural and Forest Meteorology*, *150*, 38–46.
Yang, K., Pinker, R. T., Ma, Y., Koike, T., Wonsick, M. M., Cox, S. J., et al. (2008). Evaluation of satellite estimates of downward shortwave radiation over the Tibetan Plateau. *Journal of Geophysical Research*, *113*, D17204.
Zhang, Y., Rossow, W. B., & Lacis, A. A. (1995). Calculation of surface and top of atmosphere radiative fluxes from physical quantities based on ISCCP data sets: 1. Method and sensitivity to input data uncertainties. *Journal of Geophysical Research, Atmospheres*, *100*, 1149–1165.
Zhang, Y., Rossow, W. B., Lacis, A. A., Qinas, V., & Mishchenko, M. I. (2004). Calculation of radiative fluxes from the surface to top of atmosphere based on ISCCP and other global data sets: Refinements of the radiative transfer model and the input data. *Journal of Geophysical Research, Atmospheres*, *109*, D19105.
Zhao, X., Liang, S., Liu, S., Yuan, W., Xiao, Z., Liu, Q., et al. (2013). The Global LAnd Surface Satellite (GLASS) remote sensing data processing system and products. *Remote Sensing*, *5*, 2436–2450.
Zheng, T., Liang, S., & Wang, K. (2008). Estimation of incident photosynthetically active radiation from GOES visible imagery. *Journal of Applied Meteorology and Climatology*, *47*, 853–868.